Higher-order inner photon rings of a horizonless ultracompact object with an antiphoton sphere and their interferometric pattern*

Yuan-Xing Gao (高原兴)†

Purple Mountain Observatory, Chinese Academy of Sciences, Nanjing 210023, China

Abstract: A horizonless ultracompact object can have a stable antiphoton sphere, which causes the photons inside the unstable photon sphere to strongly deflect, thereby leading to the formation of distinctive inner photon rings. In this study, we present analytical descriptions for the shape, thickness, and interference pattern of higher-order inner photon rings. By taking the static spherically symmetric Schwarzschild star with a photon sphere as an example, we find that its inner photon rings can be more non-circular and thicker than the outer ones and show that the inclusion of the inner photon rings can result in new features in the interferometric pattern. Further, our formulae can be applied to other ultracompact objects, providing a convenient approach for studying the observational properties of their higher-order photon rings.

Keywords: ultracompact object, photon ring, interferometry

DOI: 10.1088/1674-1137/addc52 **CSTR:** 32044.14.ChinesePhysicsC.49105102

I. INTRODUCTION

A black hole is a fundamental object in general relativity, and its abundance in the Universe has been demonstrated observationally, including the detection of gravitational waves from merging binary black holes [1–6] and direct images of the supermassive black holes M87* [7–12] and Sgr A* [13–18]. However, the black hole has an event horizon that blocks its connection between the interior and exterior regions, resulting in Hawking radiation, the information paradox [19, 20], and a singularity that straightforwardly causes the breakdown of general relativity. To solve these problems, ultracompact objects that possess an unstable photon sphere but no event horizon have been proposed in literature (see Ref. [21] for a review). A prominent example is the horizonless Schwarzschild star with a photon sphere, which removes the intrinsic singularity and event horizon of the Schwarzschild metric by introducing a bounded isotropic fluid into a region with a radius slightly larger than the Schwarzschild radius [22, 23].

An ultracompact object can generate unique echoes in the ringdown phase because of the absence of an event horizon [24]. Therefore, gravitational wave observations present an approach for distinguishing it from a black hole. However, it is not until the next generation of space-borne gravitational wave detectors come into operation that we can separate these echoes from the waveforms [25].

One can identify an ultracompact object by electromagnetic observations. A part of ultracompact object models have been ruled out by constraints from the size, shape, absorption, and albedo of the shadow region in the image taken by the Event Horizon Telescope [11, 18]. To further explore the possibility of the survived ones, more sophisticated data processing is required. However, given that the measurement of the shadow strongly depends on the accretion disk model [11, 17] and the accretion physics in these observations is still poorly understood, it is challenging in the current stage to obtain more precise results based only on the observed shadow.

Hidden in the image of the compact object are other subtle structures such as relativistic images and photon rings, which need to be potentially resolved by future space-borne very long baseline interferometry [26–29]. Relativistic images are formed by photons that wind around the black hole or ultracompact object one or more times before reaching the observer. Their corresponding emitters are typically point-like discrete sources such as hotspots and compact stars [30–33]. Electromagnetic signals of these images have been studied in detail [34–38]. In interferometry, the observational signatures of relativistic images exhibit an oscillating staircase-like structure,

Received 24 April 2025; Accepted 21 May 2025; Published online 22 May 2025

* Supported by the National Natural Science Foundation of China (12447143, 12273116, 62394350, and 62394351), science research grants from the China Manned Space Project (CMS-CSST-2021-A12 and CMS-CSST-2021-B10), Strategic Priority Research Program of the Chinese Academy of Sciences (XDA0350302), and Opening Project of National Key Laboratory of Aerospace Flight Dynamics of China (KGJ6142210220201)

† E-mail: gao_yx@outlook.com

which reveals their detectability with an Earth-Moon baseline [35, 37]. In comparison, photon rings arise from the lensed photons emitted by continuous extended sources such as the accretion disk [26–29, 39–42]. On the image plane of the observer, a photon ring presents a ring-shaped structure, thereby justifying the name. Photon rings are also generated by the strong deflection of photons around the black hole or ultracompact object, and therefore, they can be considered a specific realization of relativistic images. The order of a photon ring is commonly denoted by the number of half orbits n [26, 39]. Photon rings with a large n asymptotically approach the boundary of the black hole shadow [29, 43–45]. Bright thick rings surrounding M87* and Sgr A* observed by the Event Horizon Telescope can be interpreted as the lowest-order $n=0$ and $n=1$ photon rings, which are highly dependent on the accretion disk model and accretion physics [7, 13]. Higher-order photon rings ($n \geqslant 2$) can yield a good approximation of the black hole shadow border, and their shape and size are mainly determined by spacetime geometry [29]. Thus, these rings can be used to test the theory of gravity. Compared with the current direct images of the accretion disk, the $n=2$ photon ring is less dependent on the accretion model [28], which significantly reduces the number of input parameters for data interpretation and is a better tool for investigating the properties of the central compact objects.

Thus far, investigations on photon rings have been mostly numerical and computationally expensive [27–29, 40]. In comparison, the strong deflection limit method for a black hole spacetime provides a cheaper approach to analyze the properties of photon rings [32, 46], which has been successfully applied in the Schwarzschild and other black hole spacetimes [39, 41]. Further, this method is extended to the ultracompact object spacetime [33], and we make a further generalization of [33] by including the finite distance effect of a source [37]. These results present an analytical framework for investigating the difference between a black hole and an ultracompact object in photon rings.

In addition to the unstable photon sphere, an ultracompact object can have an antiphoton sphere, which has a stable circular orbit in the static spherically symmetric case [33, 36, 47–50]. Photons entering the photon sphere may be strongly deflected because of the presence of the antiphoton sphere, and then, they are received by the observer and produce inner relativistic images [33, 36–38, 49, 51] or inner photon rings [48, 52, 53]. These unique features are generally absent in black hole spacetime and thus key to distinguishing the ultracompact object from the black hole. In our previous work [37], we analytically studied the characteristics of inner relativistic images formed by point-like sources and estimated the detectability of these images. As a complement, this study focuses on the observational signatures of inner photon rings formed by photons emitted by the accretion disk, aiming to gain a batter understanding of the differences between ultracompact objects and black holes.

The shape of inner photon rings can deviate significantly from a circle and contribute moderately to the observed flux [48]. Their existence can explain the radiation in the central dark region of the images detected by the Event Horizon Telescope [18]. However, the current resolution of approximately 10 μas is insufficeint to resolve these rings because of the considerably smaller widths of inner photon rings compared to that of the primary disk and the limited interferometric baseline length, leading to a lack of detailed studies on their interferometric signatures. To address this gap, as a preliminary study, we present the analytical descriptions for the shape, thickness, and interferometric pattern of the higher-order photon rings around an ultracompact object based on the obtained results of the deflection angle by employing the strong deflection limit methods with the finite distance effect [32, 37]. In addition, this study establishes a connection between the analytical strong deflection limit method and calculation of interferometric visibility, which provides a convenient approach for exploring the observational characteristics of the ultracompact objects in the radio wavelength band.

This remainder of this paper is organized as follows. In Sec. II, we introduce photon and antiphoton spheres that are crucial for forming photon rings, and we briefly review the strong deflection limit method for an ultracompact object. Based on this method, in Sec. III, we analytically study the shape and thickness of the higher-order photon rings around an ultracompact object. In Sec. IV, we further calculate the interferometric pattern of these rings analytically and compare it with the numerical one. In Sec. V, we study the shape, thickness, and interferometric pattern of its $n=2$ inner and outer photon rings by considering a horizonless Schwarzschild star with a photon sphere as a specific example. In Sec. VI, we conclude the study and discuss our results.

II. ULTRACOMPACT OBJECT SPACETIME AND STRONGLY DEFLECTED PHOTONS

The line element of a static spherically symmetric spacetime reads

$$\mathrm{d}s^2 = -A(r)\mathrm{d}t^2 + B(r)\mathrm{d}r^2 + C(r)(\mathrm{d}\theta^2 + \sin^2\theta \mathrm{d}\phi^2), \quad (1)$$

where $A(r)$, $B(r)$, and $C(r)$ are non-negative metric functions. To describe a horizonless ultracompact object, the above metric should have no event horizon but feature a photon sphere.

In an ultracompact object spacetime, a photon can travel along a geodesic with the equation of motion

$$A(r)B(r)\,\dot{r}^2 + L^2 V_{\text{eff}\bullet} = E^2, \tag{2}$$

where E and L represent the energy and angular momentum of the photon, respectively, and they are related to the impact parameter u via [54, 55]

$$u \equiv \frac{L}{E} = \sqrt{\frac{C(r_0)}{A(r_0)}}. \tag{3}$$

where r_0 represents the turning point of the photon. The effective potential per L^2 is defined as [33]

$$V_{\text{eff}\bullet} = \frac{A(r)}{C(r)}. \tag{4}$$

An ultracompact object always has two circular orbits: one stable and the other unstable [56, 57]; they respectively correspond to the maximum and minimum of $V_{\text{eff}\bullet}$ [33].

$\mathrm{d}V_{\text{eff}\bullet}/\mathrm{d}r = 0$ and $\mathrm{d}^2V_{\text{eff}\bullet}/\mathrm{d}r^2 < 0$ define an unstable circular orbit, *i.e.*, the photon sphere [46]. We denote its radius by r_{m}. Fig. 1 shows that the photon with $r_0 \to r_{\text{m}}^+$ (*i.e.*, $r_0 > r_{\text{m}}$ and $r_0 \to r_{\text{m}}$) is strongly deflected and wound around the photon sphere several times before it is received by the observer (orange line), whereas the photon that enters the photon sphere of a black hole is absorbed by the event horizon (blue line in the first row) [46].

$\mathrm{d}V_{\text{eff}\bullet}/\mathrm{d}r = 0$ and $\mathrm{d}^2V_{\text{eff}\bullet}/\mathrm{d}r^2 > 0$ define a stable circular orbit, *i.e.*, the antiphoton sphere [33]. The stable antiphoton sphere is a unique character of the ultracompact object; however, there are few cases of black holes with

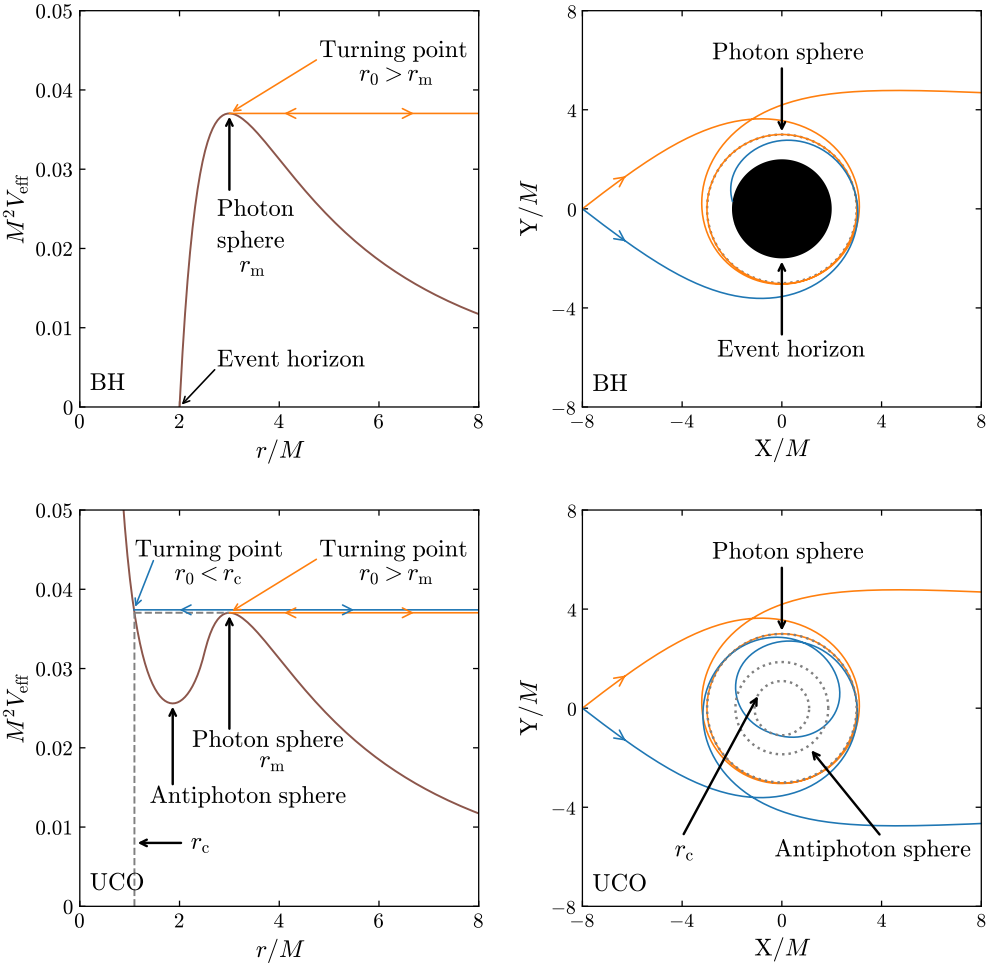

Fig. 1. (color online) Effective potential V_{eff} and photon trajectories in the black hole spacetime (first row) and ultracompact object spacetime (second row). Both the black hole and ultracompact object have a photon sphere located at $r = r_{\text{m}}$; therefore, the deflection of photons outside their photon sphere is similar (orange line). Unlike the black hole, the ultracompact object does not have an event horizon but has a unique antiphoton sphere and spherical surface $r = r_{\text{c}}$ with $V_{\text{eff}}(r_{\text{c}}) = V_{\text{eff}}(r_{\text{m}})$, which causes photons entering the photon sphere of the ultracompact object to escape (blue line). Here, we use the Schwarzschild black hole (BH) and Schwarzschild star (UCO) to illustrate and set $G = c = 1$.

an antiphoton sphere [58]. The radius of the antiphoton sphere is smaller than that of the photon sphere, and it is a key factor to imagine inside the photon sphere [33, 36, 47, 49, 50]. Owing to the existence of the antiphoton sphere, there is a radius $r_{\rm c}$ ($<r_{\rm m}$) inside the photon sphere, which satisfies

$$\frac{A(r_{\rm c})}{C(r_{\rm c})}=\frac{A(r_{\rm m})}{C(r_{\rm m})}, \tag{5}$$

or $u(r_{\rm c})=u_{\rm m}$. $r_{\rm c}$ is not the radius of the antiphoton sphere; however, it is always smaller than the latter. The blue line in Fig. 1indicates that the presence of $r_{\rm c}$ enables a photon with an impact parameter less than $u_{\rm m}$ to have a turning point of $r_0<r_{\rm m}$. This photon may escape from the interior as long as the surface of the ultracompact object does not absorb it. In the limit $r_0\to r_{\rm c}^-$ (*i.e.*, $r_0<r_{\rm c}$ and $r_0\to r_{\rm c}$), a photon can be strongly deflected [33]. An example is illustrated by the blue line in the second row of Fig. 1. Although it is true that the presence of an antiphoton sphere enables light rays to penetrate the photon sphere, the dominant contribution to the total deflection will still occur near the photon sphere.

The strong deflection of photons in the ultracompact object spacetime is related to the change in the azimuthal angle $\Delta\phi$. When the spacetime is asymptotically flat, $\Delta\phi$ is defined as [32]

$$\Delta\phi=\sum_{\rm i=S,O}\int_{r_0}^{r_{\rm i}}\sqrt{\frac{C_0A(r)B(r)}{C(r)[A_0C(r)-A(r)C_0]}}\,{\rm d}r, \tag{6}$$

where the subscript "0" denotes functions evaluated at $r=r_0$. $r_{\rm S}$ and $r_{\rm O}$ represent the radial coordinates of the source and observer, respectively. In this study, we consider that the photon is emitted by a source located outside the photon sphere (*i.e.*, a thin circular emission disk) with an initially radially-inward direction, and it can finally reach asymptotic observers [37]; therefore, we have $r_{\rm S}>r_{\rm m}$ and $r_{\rm O}\gg r_{\rm m}$. In the strong deflection limit $r_0\to r_{\rm m}^+$ and $r_0\to r_{\rm c}^-$, $\Delta\phi$ is considerably larger than 1 and can be solved analytically [32, 33, 37, 46].

A. Strong deflection of photons outside the photon sphere

In the limit of $r_0\to r_{\rm m}^+$, a photon with impact parameter $u\to u_{\rm m}^+$ winds around the gravitational lens several times before being received by the observer. Up to $O[(u-u_{\rm m})\log(u-u_{\rm m})]$, the change in the azimuthal angle of that photon can be analytically obtained as [32, 35]

$$\Delta\phi=-\bar{a}_+\log\frac{\epsilon_+}{z_{\rm O}z_{\rm S}}+\bar{b}_++\pi, \tag{7}$$

where

$$\epsilon_+=\frac{u}{u_{\rm m}}-1, \tag{8}$$

$$z_{\rm O}=1-\frac{r_{\rm m}}{r_{\rm O}},\quad z_{\rm S}=1-\frac{r_{\rm m}}{r_{\rm S}},\quad z=1-\frac{r_{\rm m}}{r}, \tag{9}$$

$$\bar{a}_+=\sqrt{\frac{2B_{\rm m}A_{\rm m}}{C_{\rm m}''A_{\rm m}-C_{\rm m}A_{\rm m}''}}, \tag{10}$$

$$\bar{b}_+=-\pi+\bar{a}_+\log\left[r_{\rm m}^2\left(\frac{C_{\rm m}''}{C_{\rm m}}-\frac{A_{\rm m}''}{A_{\rm m}}\right)\right]+\left(\int_0^{z_{\rm O}}+\int_0^{z_{\rm S}}\right)g_1(z){\rm d}z, \tag{11}$$

$$g_1(z)=\frac{r_{\rm m}}{(1-z)^2}\sqrt{\frac{C_{\rm m}A(z)B(z)}{[A_{\rm m}C(z)-A(z)C_{\rm m}]C(z)}}-\frac{\bar{a}_+}{|z|}, \tag{12}$$

The subscript "m" denotes quantities evaluated at $r=r_{\rm m}$. From Eq. (7), we can obtain the impact parameter of the strongly deflected photon outside the photon sphere as

$$u_+=u_{\rm m}\left(1+z_{\rm O}z_{\rm S}{\rm e}^{\frac{\bar{b}_++\pi-\Delta\phi}{\bar{a}_+}}\right). \tag{13}$$

B. Strong deflection of photons inside the photon sphere

In the limit $r_0\to r_{\rm c}^-$, a photon with $u\to u_{\rm m}^-$ can enter the region within the photon sphere. The photon that enters the photon sphere can reach the observer after winding around the ultracompact object several times because of the presence of the antiphoton sphere [33]. Up to $O[(u_{\rm m}^2-u^2)\log(u_{\rm m}^2-u^2)]$, the change in the azimuthal angle can be found as [37]

$$\Delta\phi=-\bar{a}_-\log\frac{\epsilon_-}{\sqrt{z_{\rm O}z_{\rm S}}}+\bar{b}_-+\pi, \tag{14}$$

where

$$\epsilon_-=\frac{u_{\rm m}^2}{u^2}-1, \tag{15}$$

$$\bar{a}_-=2\bar{a}_+, \tag{16}$$

$$\bar{b}_-=-\pi+2\bar{a}_+\log\left[2r_{\rm m}^2\left(\frac{C_{\rm m}''}{C_{\rm m}}-\frac{A_{\rm m}''}{A_{\rm m}}\right)\left(\frac{r_{\rm m}}{r_{\rm c}}-1\right)\right]+\left(\int_{1-\frac{r_{\rm m}}{r_{\rm c}}}^{z_{\rm O}}+\int_{1-\frac{r_{\rm m}}{r_{\rm c}}}^{z_{\rm S}}\right)g_1(z){\rm d}z. \tag{17}$$

Note that ϵ_- is different from ϵ_+. Although $u_{\rm m}^2/u^2-1=(u_{\rm m}/u-1)(u_{\rm m}/u+1)\approx 2(u_{\rm m}/u-1)$ can be used to make ϵ_- and ϵ_+ similar in form, this approximation can introduce a greater error, which has been discussed in Ref. [33]. From Eq. (14), we can obtain the impact parameter of the strongly deflected photon inside the photon sphere as

$$u_- = u_{\rm m}\left[1+\sqrt{z_{\rm O}z_{\rm S}}\mathrm{e}^{\frac{\bar{b}_-+\pi-\Delta\phi}{\bar{a}_-}}\right]^{-\frac{1}{2}}. \tag{18}$$

In the following sections, we use Eqs. (13) and (18) to study the shape, thickness, and interferometric pattern of higher-order photon rings.

III. INNER AND OUTER PHOTON RINGS IN THE STRONG DEFLECTION LIMIT

Considering a thin circular emission disk on the equatorial plane of an ultracompact object, the strongly deflected photons can form photon rings inside and outside the photon sphere as they are received by the observer. The inner photon rings are generally absent in black hole spacetime and therefore unique for an ultracompact object, as numerically shown in Refs. [48, 52, 53]. The order of a photon ring can be denoted by the number n of half orbits [26]. For $n\geqslant 2$, the photon wound around the ultracompact object at least once, passing through the equatorial plane more than twice, thereby generating the so-called higher-order photon rings [39].

A. Shape

The change in the azimuthal angle of the higher-order photon rings was found to be [39]

$$\Delta\phi=\begin{cases} n\pi+\gamma, & \text{for } n=2,4,6,\cdots \\ (n+1)\pi-\gamma, & \text{for } n=3,5,7,\cdots \end{cases} \tag{19}$$

where γ represents the angle between the observer and emitter in the ultracompact object-centered reference frame, given by [59]

$$\cos\gamma=\begin{cases} \dfrac{\cos\alpha}{\sqrt{\cos^2\alpha+\cot^2\vartheta_{\rm O}}}, & \text{for } n=2,4,6,\cdots \\ \dfrac{-\cos\alpha}{\sqrt{\cos^2\alpha+\cot^2\vartheta_{\rm O}}}, & \text{for } n=3,5,7,\cdots \end{cases} \tag{20}$$

with $\vartheta_{\rm O}$ being the inclination angle defined according to Ref. [39]. Here, α is not the polar angle φ normally defined counterclockwise with respect to the horizontal axis [59]. These two angles satisfy the relation [39]

$$\cos\alpha=-\sin\varphi. \tag{21}$$

Substituting the above expressions into Eqs. (13) and (18), we can obtain the impact parameter of the nth-order outer photon ring as

$$u_{+n}(\varphi)=u_{\rm m}\left[1+f_+(r_{\rm S})\mathcal{E}_{+n}(\varphi,\vartheta_{\rm O})\right], \tag{22}$$

and the impact parameter of the nth-order inner photon rings as

$$u_{-n}(\varphi)=u_{\rm m}\left[1+f_-(r_{\rm S})\mathcal{E}_{-n}(\varphi,\vartheta_{\rm O})\right]^{-\frac{1}{2}}, \tag{23}$$

where

$$f_+(r_{\rm S})=\left(1-\frac{r_{\rm m}}{r_{\rm O}}\right)\left(1-\frac{r_{\rm m}}{r_{\rm S}}\right)\exp\left[\frac{\bar{b}_+(r_{\rm S})}{\bar{a}_+}\right], \tag{24}$$

$$f_-(r_{\rm S})=\sqrt{\left(1-\frac{r_{\rm m}}{r_{\rm O}}\right)\left(1-\frac{r_{\rm m}}{r_{\rm S}}\right)}\exp\left[\frac{\bar{b}_-(r_{\rm S})}{\bar{a}_-}\right], \tag{25}$$

and

$$\begin{aligned}\mathcal{E}_{\pm n}(\varphi,\vartheta_{\rm O})=&\exp\left(\frac{1}{\bar{a}_\pm}\arccos\frac{\sin\varphi}{\sqrt{\sin^2\varphi+\cot^2\vartheta_{\rm O}}}\right)\\ &\times\exp\left(-\frac{n\pi}{\bar{a}_\pm}\right).\end{aligned} \tag{26}$$

Equation (22) agrees with Eq. (26) in Ref. [41] because both employ the same methods. $f(r_{\rm S})$ used in Ref. [39] is only valid for the Schwarzschild black hole, whereas Eq. (22) is applicable to an arbitrary black hole. Varying φ in the range $[0,2\pi]$, we can obtain the shape of the inner and outer photon rings from Eqs. (23) and (22), respectively.

B. Thickness

When the emission disk has an inner boundary $r_{\rm S}^{\rm in}$ and outer boundary $r_{\rm S}^{\rm out}$, the resulting inner or outer photon rings possess a certain thickness Δu_n. By adopting Eqs. (22) and (23), we can obtain

$$\begin{aligned}\Delta u_{+n}(\varphi)\equiv&\left|u_{+n}^{\rm out}(\varphi)-u_{+n}^{\rm in}(\varphi)\right|\\ =&u_{\rm m}\left[f_+(r_{\rm S}^{\rm out})-f_+(r_{\rm S}^{\rm in})\right]\mathcal{E}_{+n}(\varphi,\vartheta_{\rm O}),\end{aligned} \tag{27}$$

for the nth-order outer rings, and

$$\Delta u_{-n}(\varphi)\equiv\left|u_{-n}^{\rm out}(\varphi)-u_{-n}^{\rm in}(\varphi)\right|$$

$$= u_{\rm m}\left\{\left[1+f_{-}(r_{\rm S}^{\rm in})\mathcal{E}_{-n}(\varphi,\vartheta_{\rm O})\right]^{-\frac{1}{2}} - \left[1+f_{-}(r_{\rm S}^{\rm out})\mathcal{E}_{-n}(\varphi,\vartheta_{\rm O})\right]^{-\frac{1}{2}}\right\}, \tag{28}$$

for the nth-order inner rings. Eq. (27) is a direct generalization of corresponding equations in Ref. [39].

IV. INTERFEROMETRIC PATTERN OF THE INNER AND OUTER PHOTON RINGS

Higher-order photon rings can be detected by very long baseline interferometry [27]. The interferometric signature of a photon ring is its visibility, which can be defined as a Fourier transform [60]

$$\mathcal{V}(\vec{\rm u}) = \int I(\vec{r})\mathrm{e}^{-\mathrm{j}2\pi\vec{\rm u}\cdot\vec{r}}\mathrm{d}^2\vec{r}, \tag{29}$$

where $I(\vec{r})$ represents the intensity distribution of the photon ring, $\vec{r}=(x,y)$ represents the sky position in radians, and $\vec{\rm u}$ represents the baseline vector in units of the observed wavelength λ.

The calculation of $\mathcal{V}(\vec{\rm u})$ requires a complete two-dimensional Fourier transform that involves large computational costs. However, for image reconstruction, we can first cut one-dimensional slices of the visibility in different directions and then combine them to obtain two-dimensional visibility, which is the basic idea of the projection-slice theorem [60].

To apply this theorem, we denote $\vec{\rm u}=({\rm u},\sigma)$ in polar coordinates, where σ and u represent the projection angle and projected length of the baseline in the direction of σ, respectively. The projection axis is rotated clockwise by the angle of σ to make it horizontal for mathematical convenience. Then, the sky coordinates of a photon ring can be written as

$$x(\varphi) = u(\varphi)\cos(\varphi-\sigma), \tag{30}$$

$$y(\varphi) = u(\varphi)\sin(\varphi-\sigma). \tag{31}$$

Here, we omit the subscript "±" of $u(\varphi)$ and note that the following calculations are applied for both the inner and outer photon rings. Further, to obtain $\vec{r}=(x,y)$ in radians, we divide u by the distance from the lens to the observer.

We can use arclength $\tilde{s}$ to parametrize the shape curve of the photon ring as $u(\varphi)=u(\tilde{s})=(x(\tilde{s}),y(\tilde{s}))$. When the baseline is not long enough to resolve the thickness of a photon ring, *i.e.*,

$${\rm u} \ll (\Delta u)^{-1}, \tag{32}$$

the projection of the intensity distribution on the horizontal axis may be given by [61]

$$\mathcal{P}_x I(x) = \int \mathcal{I}(\tilde{s})\delta(x-x_0(\tilde{s}))\mathrm{d}\tilde{s} = \sum_{x=x_0}\frac{\mathcal{I}}{\mathrm{d}x_0/\mathrm{d}\tilde{s}}. \tag{33}$$

where $\mathcal{I}(\tilde{s})$ represents the integrated intensity for a photon ring with uniform brightness, and we have $\mathcal{I}(\tilde{s})=I_0=I_{\rm tot}/\int\mathrm{d}\tilde{s}$. x_0 represents the point where the vertical line intersects the shape curve.

For $\mathrm{d}x_0/\mathrm{d}\tilde{s}=0$, the vertical line is tangent to the shape curve, and we denote the corresponding x_0 as the tangential point $x_{\rm T}$ (*i.e.*, the vertical point of tangency). From Eq. (33), we know that the projection intensity $\mathcal{P}_x I(x)$ becomes singular at $x=x_{\rm T}$, which implies that the behavior of the resulting visibility is dominated by tangential points [61].

To find out the positions of all tangential points on the shape curve, we rewrite the infinitesimal arclength as

$$\mathrm{d}\tilde{s} = \sqrt{x'(\varphi)^2+y'(\varphi)^2}\,\mathrm{d}\varphi = \sqrt{u(\varphi)^2+u'(\varphi)^2}\,\mathrm{d}\varphi \neq 0, \tag{34}$$

where the prime indicates the derivative with respect to φ. Meanwhile, by adopting the chain rule, we have

$$\frac{\mathrm{d}x_0}{\mathrm{d}s} = \frac{\mathrm{d}x_0}{\mathrm{d}\varphi}\frac{\mathrm{d}\varphi}{\mathrm{d}s}. \tag{35}$$

Then, the condition of $\mathrm{d}x_0/\mathrm{d}\tilde{s}=0$ can be converted to $\frac{\mathrm{d}x_0}{\mathrm{d}\varphi}\big|_{x_0=x_{\rm T}}=0$. Further, with Eq. (30), we have

$$\mathcal{F}(\varphi_{\rm T}) = u'(\varphi_{\rm T})\cos(\varphi_{\rm T}-\sigma) - u(\varphi_{\rm T})\sin(\varphi_{\rm T}-\sigma) = 0, \tag{36}$$

where $\varphi_{\rm T}$ represents the corresponding polar angle of $x_{\rm T}$ and its value can be obtained from Eq. (36) by employing a FindRoot algorithm.

From Eq. (30), we can further obtain $x_{\rm T}$. Then, $\mathcal{P}_x I(x)$ in the small two-sided neighborhood of $x_{\rm T}$ can be approximated by the Heaviside step functions (see Eq. (28) in Ref. [61]). The Fourier transfrom of the approximated $\mathcal{P}_x I(x)$ yields the visibility [61]

$$\mathcal{V}({\rm u},\sigma) = \sum_{x=x_{\rm T}}\mathcal{I}_{\rm T}\sqrt{\mathcal{R}_{\rm T}}\,\mathrm{e}^{-\mathrm{j}\frac{\pi}{4}S_{\rm T}}\frac{\mathrm{e}^{-\mathrm{j}2\pi\mathcal{Z}_{\rm T}{\rm u}}}{\sqrt{\rm u}}, \tag{37}$$

where subscript "T" represents quantities evaluated at

$x = x_{\rm T}$, and $\mathcal{I}_{\rm T}$ represents the integrated intensity. $S_{\rm T} = \pm 1$ depending on whether the horizontal axis and inward normal vector (pointing to the curvature center) at the tangential point are in the same (+1) or opposite (−1) direction. $\mathcal{Z}_{\rm T}$ represents the projected position of the tangential point on the horizontal axis. According to the definition in Ref. [61], the projected position of a point on the shape curve can be written as

$$\mathcal{Z}(\sigma') = x(\varphi)\cos(\sigma') + y(\varphi)\sin(\sigma'). \tag{38}$$

For the horizontal projection axis, we have $\sigma' = 0$, and thus, we obtain

$$\mathcal{Z}_{\rm T} = x_{\rm T}(\varphi_{\rm T}). \tag{39}$$

$\mathcal{R}_{\rm T}$ represents the curvature radius [61] given by

$$\mathcal{R}_{\rm T} = \left| \sqrt{[x'(\varphi)]^2 + [y'(\varphi)]^2}\, \frac{{\rm d}\varphi}{{\rm d}\sigma'} \right|_{\varphi=\varphi_{\rm T}}. \tag{40}$$

By taking the derivative of Eq. (38) with respect to φ, we can obtain [62]

$$\tan(\sigma') = -\frac{x'(\varphi)}{y'(\varphi)}, \tag{41}$$

which enables us to further compute

$$\mathcal{R}_{\rm T} = \frac{\left[y'(\varphi_{\rm T})\right]^2}{\left|x''(\varphi_{\rm T})\right|}. \tag{42}$$

Here, we used the condition $x'(\varphi_{\rm T}) = 0$.

To sum up, in regime (32), the final expression (37) for the visibility of the outer or inner higher-order photon rings is proposed by Ref. [61]. By adopting the strong deflection limit method, we find that the coefficients included can be simply evaluated with the help of Eqs. (36), (39), and (42).

V. APPLICATIONS TO SPECIFIC ULTRACOMPACT OBJECTS

In this study, we consider the Schwarzschild star with a photon sphere as a simple example although our formulae can be applied to other ultracompact objects.

The Schwarzschild star is an isotropic self-gravitating object with a uniform energy density, which is an exact solution of general relativity [63]. Although suffering from the Buchdahl limit [64] and oversimplified uniform matter distribution, the Schwarzschild star has attracted considerable attention regarding its anisotropy [65, 66], time dependence [67], connection to the gravastar [68, 69], nonvanishing positive tidal Love number [70], and power-law tail that is very similar to the Schwarzschild black hole in the gravitational wave ringdown waveform [71]. Besides, the Schwarzschild star may be the simplest model for studying the common features of ultracompact objects.

The explicit form of the Schwarzschild star metric is given by ($G = c = 1$) [22, 23, 33, 37]

$$A(r) = \begin{cases} \left(\frac{3}{2}\sqrt{\mathcal{H}_R} - \frac{1}{2}\sqrt{\mathcal{H}_r}\right)^2, & r < R, \\ 1 - \frac{R_{\rm s}}{r}, & r \geqslant R, \end{cases} \tag{43}$$

$$B(r) = \begin{cases} \mathcal{H}_r^{-1}, & r < R, \\ \left(1 - \frac{R_{\rm s}}{r}\right)^{-1}, & r \geqslant R, \end{cases} \tag{44}$$

$$C(r) = r^2, \tag{45}$$

where $R_{\rm s} = 2M$ represents the Schwarzschild radius, and M represents the ADM mass. Further, R represents the radius of the Schwarzschild star, and its value is constrained by Buchdahl's theorem [64]. $\mathcal{H}_R$ and $\mathcal{H}_r$ are respectively defined as

$$\mathcal{H}_R = 1 - \frac{R_{\rm s}}{R}, \tag{46}$$

$$\mathcal{H}_r = 1 - \frac{R_{\rm s}}{R^3} r^2. \tag{47}$$

We assume that the Schwarzschild star does not emit electromagnetic waves itself and has an electromagnetically transparent surface with a relatively high absorption rate in its interior [21, 37, 72]. Subsequently, its optical appearance may have a dark spot in the center that is consistent with current observed images taken by the Event Horizon Telescope [12, 18]. In this scenario, photons can enter the region where $r < R$, thereby providing the possibility for forming inner photon rings.

For a Schwarzschild star with $9R_{\rm s}/8 < R < 3R_{\rm s}/2$, it is shown that the geodesic equation (2) is well-defined under the above assumptions, and the lensed photons entering the photon sphere can reach an observer [37]. In this configuration, the photon sphere is located at

$$r_{\rm m} = \frac{3}{2}R_{\rm s}, \tag{48}$$

and the antiphoton sphere locates at [37]

$$r_{\rm a}=\frac{(R/R_{\rm s})^{3/2}}{3}\sqrt{\frac{8R/R_{\rm s}-9}{R/R_{\rm s}-1}}R_{\rm s}. \tag{49}$$

From Eq. (5), we can find [37]

$$r_{\rm c}=\frac{3\sqrt{3}R}{16(R/R_{\rm s})^3+27}\left[12\sqrt{(R/R_{\rm s})^4-(R/R_{\rm s})^3}\right.$$
$$\left.-\sqrt{16(R/R_{\rm s})^4-216(R/R_{\rm s})+243}\right]. \tag{50}$$

By taking the Schwarzschild star with $R=2.5M$ as an example, we evaluate the accuracy of Eqs. (13) and (18). Their error with respect to numerical results increases with a decrease in$\Delta\phi$, and the relative error of u_- is considerably larger than that of u_+. For $\Delta\phi\geqslant 2\pi$ (always satisfied for higher-order photon rings; see Eq. (19)), we find that u_- has the largest relative error that is approximately 7% when $\Delta\phi=2\pi$; however, this value reduces to 0.6% when $\Delta\phi$ increases to 3π. These errors are reasonably accepted in this work.

With Eqs. (23) and (22), we show the shape curves of the $n=2,3$ inner and outer photon rings in Fig. 2. The $n=2$ inner ring is nearly circular for a low inclination ($\vartheta_{\rm O}=17^\circ$); however, its lower half can be clearly deformed for a high inclination ($\vartheta_{\rm O}=85^\circ$). The same is true for the $n=3$ inner ring, whereas the shape curve is always nearly circular for the $n=2$ or 3 outer ring. The term ``nearly" is adopted here because the lower half of the outer photon ring can deviate from a circular shape slightly when the inclination angle is high. Fig. 2 shows that the inner photon rings gradually approach the image center with an increase in the radius $r_{\rm S}$ of the emission disk.

Then, we use Eqs. (28) and (27) to obtain the thicknesses of the $n=2,3$ inner and outer photon rings of the Schwarzschild star with $R=2.5M$. The results are shown in Fig. 3. Here, we set $r_{\rm S}^{\rm in}=3.1M$ and $r_{\rm S}^{\rm out}=20M$ and show the thicknesses of the $n=2,3$ inner and outer photon rings of the Schwarzschild star with $R=2.5M$. We find that the thicknesses of these photon rings satisfy the relationship of $\Delta u_{-2}>\Delta u_{-3}>\Delta u_{+2}>\Delta u_{+3}$, and the thickness of the inner rings has a maximum at $\varphi=3\pi/2$, similar to that of the outer ones [39].

To compute the visibility of the higher-order inner and outer photon rings, we first need to determine the location of the tangential points on the shape curve by using Eq. (36). Assuming that the mass and distance of the Schwarzschild star with $R=2.5M$ are the same as M87* [12] and the inclination of the surrounding thin circular disk with $r_{\rm S}=20M$ is $\vartheta_{\rm O}=85^\circ$, we show the $\mathcal{F}(\varphi)$ of the $n=2$ inner photon ring in Fig. 4. The roots of $\mathcal{F}(\varphi)$ yield the $\varphi_{\rm T}$ of the tangential points, marked by the orange solid dots. We find that the number of the tangential points is 2 for $\sigma=0^\circ$ or 90°, whereas the number is 4 for $\sigma=45^\circ$ or 135°. The locations of these tangential points on the shape curves are shown in the first column of Fig. 5. Further, we find that the number of the tangential

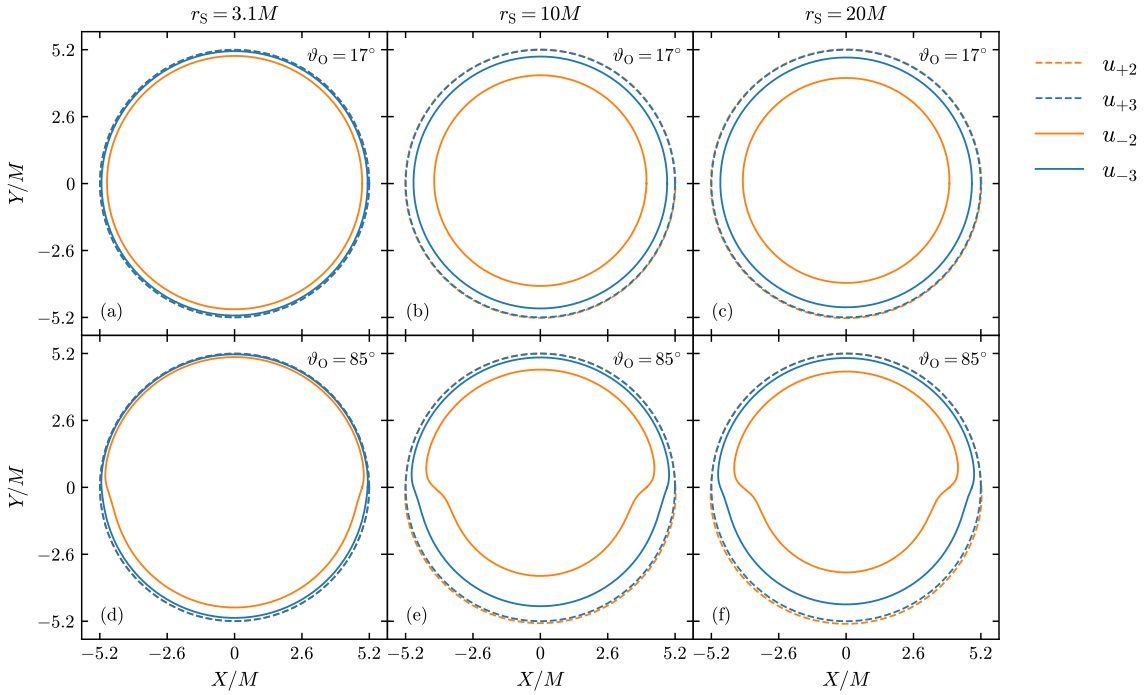

Fig. 2. (color online) Shape curves of the $n=2,3$ inner and outer photon rings of the Schwarzschild star with radius $R=2.5M$. From the first column to the third column, the radius $r_{\rm S}$ of the thin circular emission disk is $3.1M, 10M, 20M$, respectively. The inclination angle $\vartheta_{\rm O}$ is 17° in the first row and 85° in the second row.

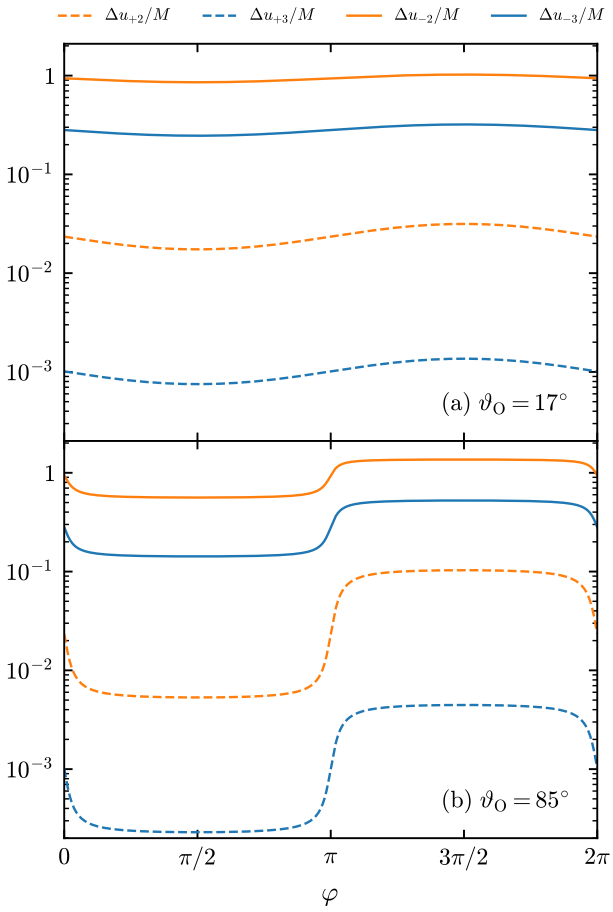

Fig. 3. (color online) Thicknesses of the $n = 2,3$ inner and outer photon rings of the Schwarzschild star with radius $R = 2.5M$, given a thin circular emission disk with inner boundary $r_S^{in} = 3.1M$ and outer boundary $r_S^{out} = 20M$. (a) The inclination angle $\vartheta_O = 17°$ and (b) $\vartheta_O = 85°$.

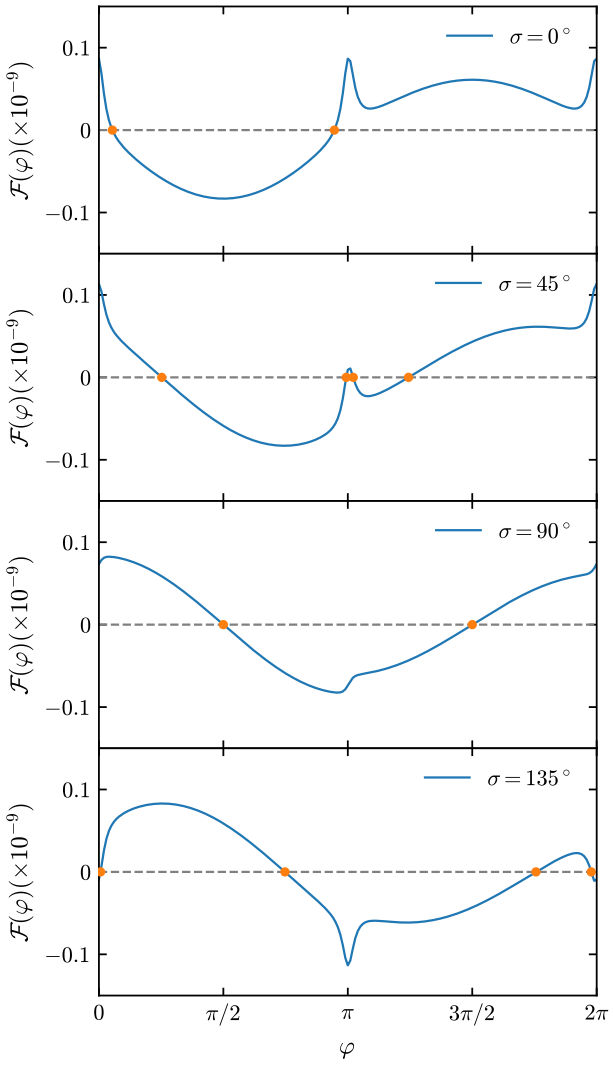

Fig. 4. (color online) $\mathcal{F}(\varphi)$ of the $n = 2$ inner photon ring. From top to bottom, the projection angle σ is respectively $0°, 45°, 90°, 135°$. The gravitational lens is assumed to be a $R = 2.5M$ Schwarzschild star with mass and distance equal to M87*. The light source is a thin circular emission disk with radius $r_S = 20M$ and inclination $\vartheta_O = 85°$. The orange solid dots mark the φ_T of the tangential points.

points of the $n = 2$ outer photon ring is always 2, and they show their locations on the shape curves in the first column of Fig. 6.

In the second column of Figs. 5 and 6, for each σ, we use the blue solid line to show the normalized projected intensity $P_x I_{norm} = P_x I/(P_x I)_{max}$, which is obtained by adopting a numerical Radon transform algorithm [29], *i.e.*, the complete integral of the intensity I along vertical lines. On the horizontal axis, we use the orange solid dots to mark the positions of x_T. $P_x I_{norm}$ indeed has a singular behavior at $x = x_T$, which agrees with the previous discussion. Further, we find that $\mathcal{P}_x I_{norm}$ of the $n = 2$ inner photon ring has additional substructures in $|x| < |x_T|$ for $\sigma = 0°$, which can produce a subdominant term of the visibility and are beyond the prediction of Eq. (37).

In the third column of Figs. 5 and 6, we use the blue solid line to show the (normalized) visibility $\mathcal{V}(u,\sigma)$ corresponding to the numerical $P_x I_{norm}$ for each σ, and we use the orange solid line to show the (normalized) visibility given by our formulae. The oscillating phase of $\mathcal{V}(u,\sigma)$ given by our formulae coincides exactly with that of the numerical $\mathcal{V}(u,\sigma)$, whereas its amplitude can be different from that of the numerical one, as illustrated in the first, second, and fourth rows of Fig. 5. The reason can include the following two aspects. (1) The $n = 2$ inner photon ring can have substructures that are not contained in Eq. (37) (for the case of $\sigma = 0°$), which produces unpredicted additional interference envelopes in $\mathcal{V}(u,\sigma)$. (2) The numerical algorithm undersamples in the neighborhood of x_T (for $\sigma = 45°$ and $135°$), which makes the integral intensity differ from the prediction of Eq. (37) and further affect the normalization of $\mathcal{V}(u,\sigma)$. These discrepancies are reduced when the overall visibil-

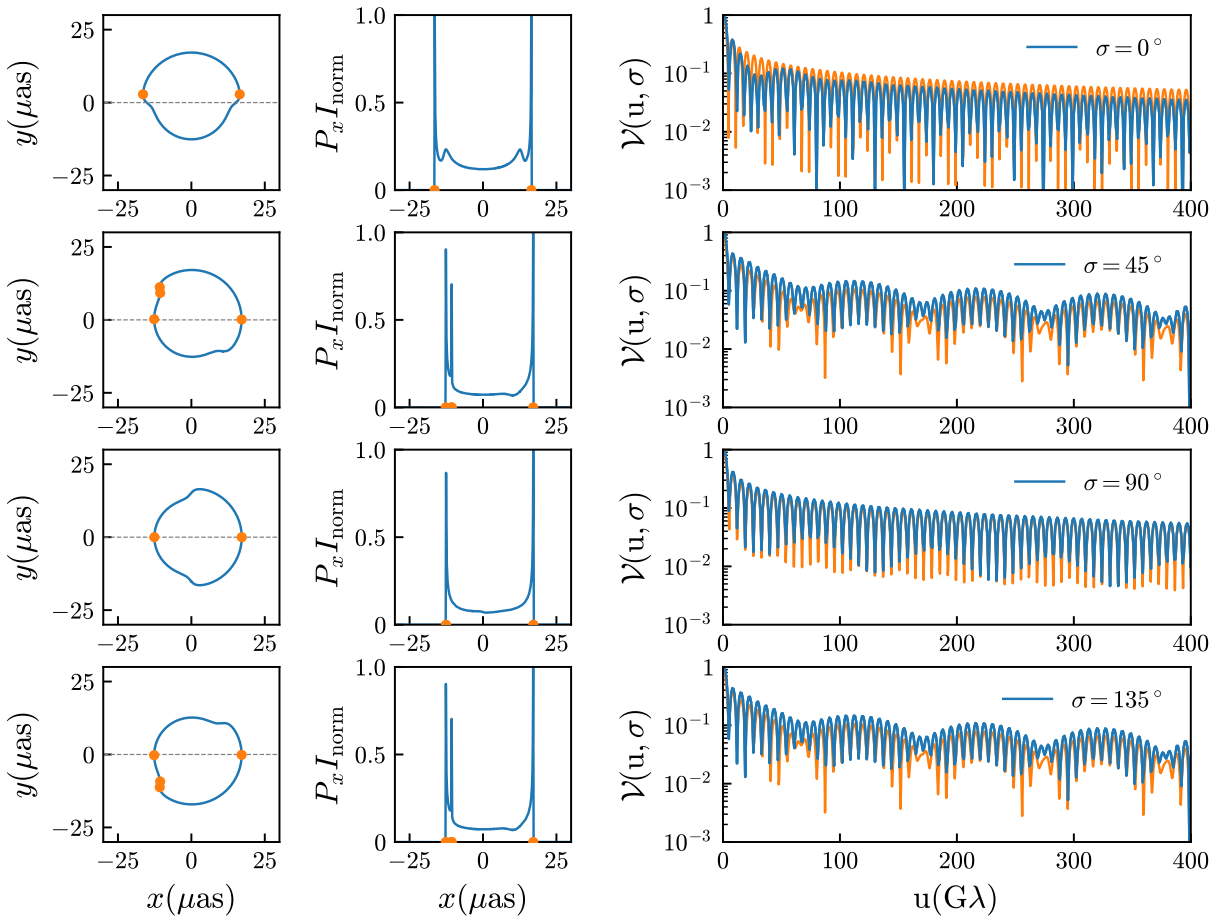

Fig. 5. (color online) Shape curve, normalized projected intensity $P_x I_{\rm norm}$, and (normalized) visibility $\mathcal{V}(u,\sigma)$ of the $n=2$ inner photon ring. The lens is assumed to be a $R=2.5M$ Schwarzschild star with mass and distance equal to M87*. The source is a thin circular emission disk with radius $r_S=20M$ and inclination $\vartheta_O=85°$. The blue solid lines represent numerical results (Radon transform for $P_x I_{\rm norm}$ and Fourier transform for $\mathcal{V}$). The orange solid dots mark the positions of the tangential points, and the orange solid line represents the visibility given by our formulae.

ity of multiple photon rings is considered, which indicates that the superposition of singular tangential points from different photon rings can weaken the effects of substructures and undersampling.

Based on the current observational results of M87* and Sgr A*, their photon rings should be nearly circular since the observational inclinations are both estimated to be low [17]. For these two objects, the number of the tangential points would always be 2, and there would be no distinct additional substructures in the intensity profile. Therefore, we expect that $\mathcal{V}(u,\sigma)$ given by Eq. (37) can approximate the actual visibility of the higher-order photon rings very well.

From Fig. 5, we find that $\mathcal{V}(u,\sigma)$ of the $n=2$ inner photon ring may have different characteristics based on σ. For $\sigma=0°$ and $90°$, the only two tangential points lead to the fact that $\mathcal{P}_x I_{\rm norm}$ is very similar to that of a circular ring, and therefore, the resulting $\mathcal{V}(u,\sigma)$ behaves like a cosine function. For $\sigma=45°$ and $135°$, distinct envelopes may appear because of the presence of four tangential points, which are absent in $\mathcal{V}(u,\sigma)$ of the outer photon ring and provide some evidence for the existence of the Schwarzchild star. The first envelope appears at a position of approximately 100Gλ. Given that the intensity of the photon rings decreases exponentially with an increase in the order n, the width effect causes the visibility modulus to exhibit a staircase-like shape where lower-order photon rings dominate higher steps [27]. The observability of the $n=2$ inner photon ring at 100Gλ will be crucial for distinguishing the ultracompact object from the black hole. Although the current observational capability of the Event Horizon Telescope is approximately 10Gλ [13], in future, it is highly promising to achieve resolutions corresponding to several tens to 100Gλ, with the frequency upgrade of the next-generation event horizon telescope [28, 29, 73] or the realization of the space-borne very long baseline interferometry with a baseline equivalent to the Earth-Moon distance [27, 37]. Meanwhile, it is very likely to distinguish the photon-ring differences between the ultracompact object and the black

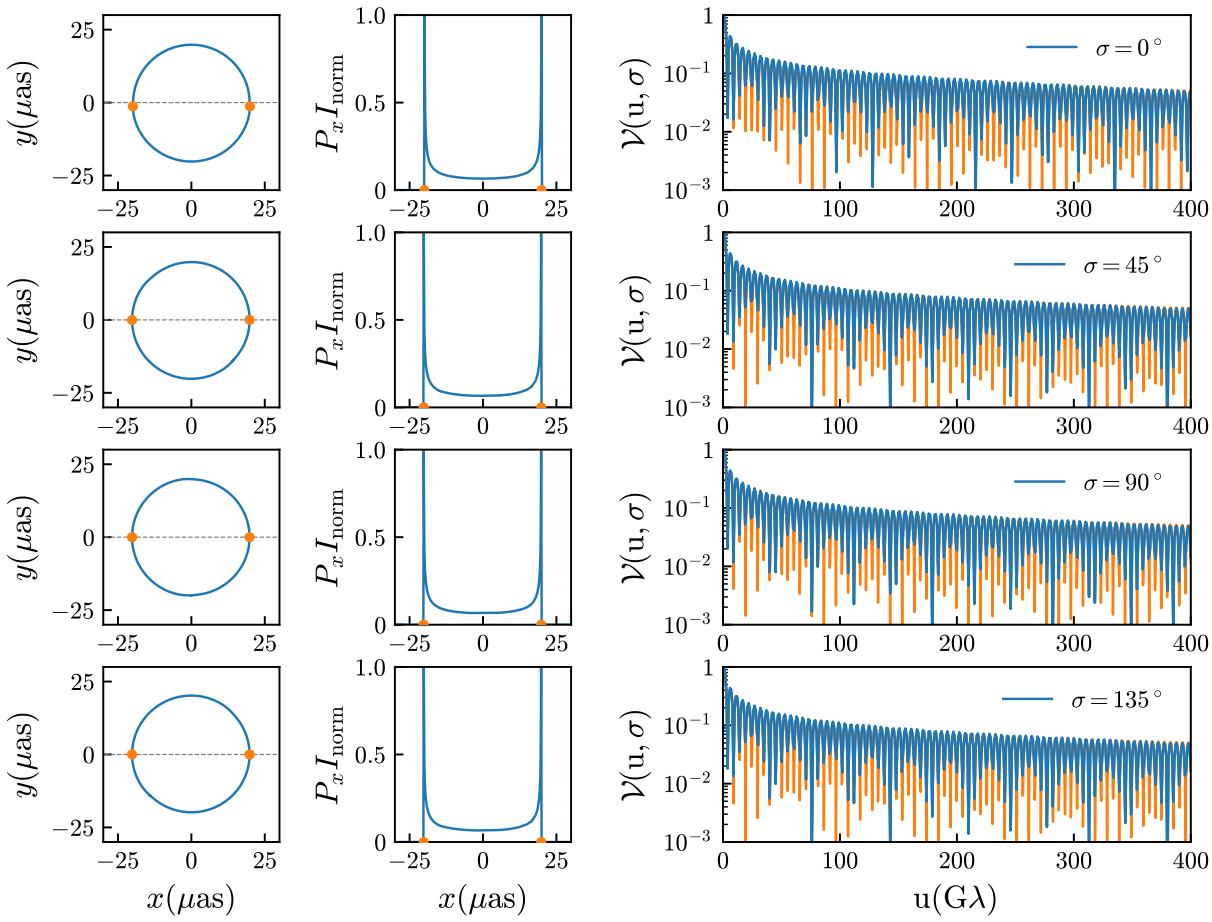

Fig. 6. (color online) Shape curve, normalized projected intensity $P_x I_{\rm norm}$, and (normalized) visibility $\mathcal{V}(u,\sigma)$ of the $n=2$ outer photon ring. The physical setup and color representation are the same as in Fig. 5.

hole at 100 Gλ in the visibility regime.

A. Overall visibility of the inner and outer photon ring pairs

An ultracompact object has at least an unstable photon sphere and a stable antiphoton sphere [56, 57], which leads to Eq. (5) being satisfied. In terms of the effective potential, strongly deflected photons will be present inside the photon sphere when there are strongly deflected photons outside the photon sphere. Therefore, the inner and outer photon rings will appear simultaneously for an ultracompact object. Motivated by this, we show the overall visibility of the $n=2$ inner and outer photon rings in Fig. 7. Here, we assume that the integrated intensity on the shape curves is equal everywhere, *i.e.*, $\mathcal{I}(s)=1$.The overall visibility given by our formulae are still in good agreement with the numerical ones. This good match indicates that we can potentially generalize our results to approximate the visibility of a photon ring with a thickness by superimposing the tangential points of different photon rings.

Further, we find that the overall visibility becomes more complicated than the individual inner one shown in Fig. 5 (or outer one shown in Fig. 6). However, given that the intensity of an inner ring would be considerably different from that of an outer ring because of the effect of gravitational lensing and gravitational redshift [26, 33, 36, 49]. The thickness of a photon ring may cause its intensity profile to decrease exponentially [27, 40]; the actual overall visibility may be simplified with a staircase-like structure.

Finally, we give $\{\mathcal{I}_{\rm T}, \mathcal{R}_{\rm T}, \mathcal{S}_{\rm T}, \mathcal{Z}_{\rm T}\}$ for the visibility of the $n=2$ and 3 photon rings of the Schwarzschild star with radius $R=2.5M$ in Tables 1 and 2, respectively. In addition, the visibility of the $n=3$ inner and outer photon rings are shown in Appendix. A.

VI. CONCLUSIONS AND DISCUSSION

Horizonless ultracompact objects are a class of black hole mimickers that possess an unstable photon sphere. The accretion disk around an ultracompact object can form outer photon rings under strong deflection gravitational lensing, similar to a black hole. However, unlike the black hole, the ultracompact object can have a stable

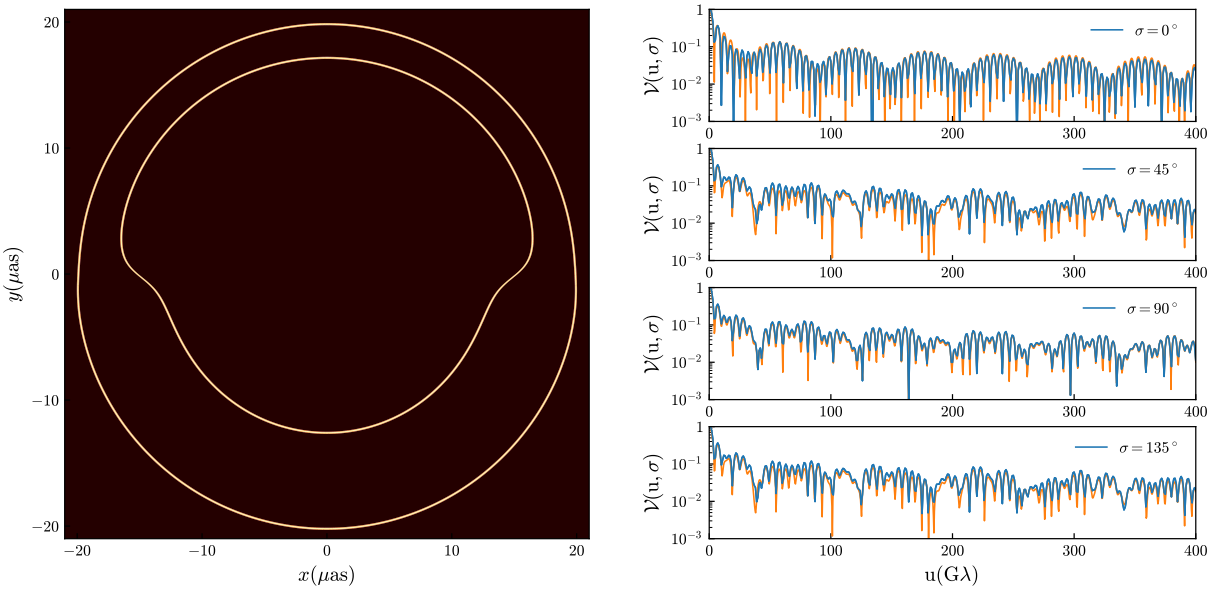

Fig. 7. (color online) Overall (normalized) visibility $\mathcal{V}(u,\sigma)$ of the $n=2$ inner and outer photon rings. The physical setup and color representation is the same as in Fig. 5. The integrated intensities of the inner and outer rings are assumed to be identical.

antiphoton sphere, which gives rise to distinctive inner photon rings. These inner rings are key to distinguishing the ultracompact object from the black hole.

In this paper, we present the analytical descriptions of the shape, thickness, and interferometric pattern of the inner and outer higher-order photon rings around an ultracompact object that has an unstable photon sphere but no event horizon. These descriptions are based on the strong deflection limit method with the finite distance effect for the black hole [32] and ultracompact object [37], which provides a convenient approcah for exploring the observational characteristics of the ultracompact objects in the radio wavelength band.

Considering the Schwarzschild star with radius $R=2.5M$ as the gravitational lens and a thin circular emission disk on its equatorial plane, we find the following:

(1) The $n=2$ inner and outer photon rings are nearly circular for a low inclination.

(2) The lower half of the $n=2$ inner ring can be clearly deformed for a high inclination.

(3) The nth-order inner ring is always thicker than the nth-order outer ring.

(4) The phase of visibility is exactly determined by the tangential points on the shape curve of a photon ring.

(5) The $n=2$ inner ring has more distinct features in both intensity profile and visibility than the $n=2$ outer ring, and it can generate new envelopes in the visibility for a high inclination. These new envelopes have the potential to be detected by the Earth-Moon baseline interferometry.

(6) By using the strong deflection limit approach, we can quickly and efficiently generate the interferometric pattern of the higher-order photon rings, which can match

Table 1. $\{\mathcal{I}_T, \mathcal{R}_T, \mathcal{S}_T, \mathcal{Z}_T\}$ for the visibility of the $n=2$ photon rings of the Schwarzschild star with radius $R=2.5M$.

		$n=2$	
		Inner ring	Outer ring
$\sigma=0°$	$\mathcal{I}_T$	(1,1)	(1,1)
	$\mathcal{R}_T(\times10^{-9})$	(0.0304,0.0304)	(0.0791,0.0791)
	$\mathcal{S}_T$	(−1,1)	(1,1)
	$\mathcal{Z}_T(\times10^{-9})$	(0.0798,−0.0798)	(0.0967,−0.0967)
$\sigma=45°$	$\mathcal{I}_T$	(1,1,1,1)	(1,1)
	$\mathcal{R}_T(\times10^{-9})$	(0.0812,0.0249,0.0209,0.0652)	(0.0962,0.0973)
	$\mathcal{S}_T$	(−1,1,−1,1)	(−1,1)
	$\mathcal{Z}_T(\times10^{-9})$	(0.0830,−0.0515,−0.0522,−0.0614)	(0.0962,−0.0979)
$\sigma=90°$	$\mathcal{I}_T$	(1,1)	(1,1)
	$\mathcal{R}_T(\times10^{-9})$	(0.0827,0.0619)	(0.0962,0.0978)
	$\mathcal{S}_T$	(−1,1)	(1,1)
	$\mathcal{Z}_T(\times10^{-9})$	(0.0832,−0.0611)	(0.0962,−0.0980)
$\sigma=135°$	$\mathcal{I}_T$	(1,1,1,1)	(1,1)
	$\mathcal{R}_T(\times10^{-9})$	(0.0812,0.0249,0.0209,0.0652)	(0.0962,0.0973)
	$\mathcal{S}_T$	(−1,1,−1,1)	(−1,1)
	$\mathcal{Z}_T(\times10^{-9})$	(0.0830,−0.0515,−0.0522,−0.0614)	(0.0962,−0.0979)

Table 2. $\{\mathcal{I}_{\rm T}, \mathcal{R}_{\rm T}, \mathcal{S}_{\rm T}, \mathcal{Z}_{\rm T}\}$ for the visibility of the $n=3$ photon rings of the Schwarzschild star with radius $R=2.5M$.

		$n=3$	
		Inner ring	Outer ring
$\sigma=0°$	$\mathcal{I}_{\rm T}$	$(1,1)$	$(1,1)$
	$\mathcal{R}_{\rm T}(\times10^{-9})$	$(0.0388,0.0388)$	$(0.0986,0.0986)$
	$\mathcal{S}_{\rm T}$	$(-1,1)$	$(-1,1)$
	$\mathcal{Z}_{\rm T}(\times10^{-9})$	$(0.0913,-0.0913)$	$(0.0961,-0.0961)$
$\sigma=45°$	$\mathcal{I}_{\rm T}$	$(1,1)$	$(1,1)$
	$\mathcal{R}_{\rm T}(\times10^{-9})$	$(0.0923,0.0861)$	$(0.0961,0.0961)$
	$\mathcal{S}_{\rm T}$	$(-1,1)$	$(-1,1)$
	$\mathcal{Z}_{\rm T}(\times10^{-9})$	$(0.0928,-0.0842)$	$(0.0960,-0.0961)$
$\sigma=90°$	$\mathcal{I}_{\rm T}$	$(1,1)$	$(1,1)$
	$\mathcal{R}_{\rm T}(\times10^{-9})$	$(0.0927,0.0845)$	$(0.0960,0.0961)$
	$\mathcal{S}_{\rm T}$	$(-1,1)$	$(1,1)$
	$\mathcal{Z}_{\rm T}(\times10^{-9})$	$(0.0929,-0.0841)$	$(0.0960,-0.0961)$
$\sigma=135°$	$\mathcal{I}_{\rm T}$	$(1,1)$	$(1,1)$
	$\mathcal{R}_{\rm T}(\times10^{-9})$	$(0.0923,0.0861)$	$(0.0961,0.0961)$
	$\mathcal{S}_{\rm T}$	$(-1,1)$	$(-1,1)$
	$\mathcal{Z}_{\rm T}(\times10^{-9})$	$(0.0928,-0.0842)$	$(0.0960,-0.0961)$

the numerical result well.

We do not consider the spin effect of the spacetime because the analytical method is established within the spherically symmetric framework. The numerical results show that such an effect on the shape and other properties of the photon rings should be small [28, 29, 74]. However, the spin of the spacetime still holds profound theoretical and observational significance. For example, the frame-dragging effect attributed to the spin can induce significant azimuthal rotation within different levels of photon rings and echo signals [75, 76], which may lead to new features in the corresponding interferometric signatures. To include the spin effect, the key elements of analytical studies are the analytical metric describing a spinning ultracompact object [77–81] and the analytical approximation for light deflection in the spinning ultracompact object spacetime. However, the latter is still under development up to now [82], which means that constructing the shape curves of higher-order photon rings of the spinning ultracompact object can only rely on numerical algorithms at present [83].

Once the shape curves of the inner and outer photon rings around a spinning ultracompact object are obtained, we can still use the visibility approximation (37) for generating the interferometric pattern because it is applicable to closed curves with an arbitrary shape [61]. We expect that the introduction of the spin effect will not change its form and instead only change the number of tangential points. However, according to the thickness analysis in Sec. III, it can be easy to go beyond the regime (32). That is, the baseline length u needs to be smaller than $50{\rm G}\lambda$ (that roughly corresponds to the thickness of $1M$) for the $n=2$ inner photon ring. Thus, Eq. (37) should be generalized for ${\rm u}>50{\rm G}\lambda$, which deserves future work.

The overall visibility of the outer photon rings is staircase-like because of their different intensities [27, 40]. The $n=1$ outer ring dominates the highest step, the $n=2$ outer ring dominates the second highest step, and so on. The presence of the inner photon rings can change these relationships. Our analytical formulae provide a computationally inexpensive approach to study the correspondence between the visibility step height and order of the photon ring; this will be our next move.

ACKNOWLEDGEMENTS

We thank Prof. Yi Xie for helpful discussions.

APPENDIX A: PROJECTED INTENSITY $P_x I_{\rm norm}$ AND CORRESPONDING VISIBILITY OF THE $n=3$ PHOTON RINGS

In Fig. A1, we show the shape curve, normalized projected intensity $P_x I_{\rm norm}$, and (normalized) visibility $\mathcal{V}({\rm u},\sigma)$ of the $n=3$ inner ring, and in Fig. A2, we show those of the $n=3$ outer ring. Table 2 presents the $\{\mathcal{I}_{\rm T}, \mathcal{R}_{\rm T}, \mathcal{S}_{\rm T}, \mathcal{Z}_{\rm T}\}$ values for the visibility of the $n=3$ photon rings around the Schwarzschild star with $R=2.5M$.

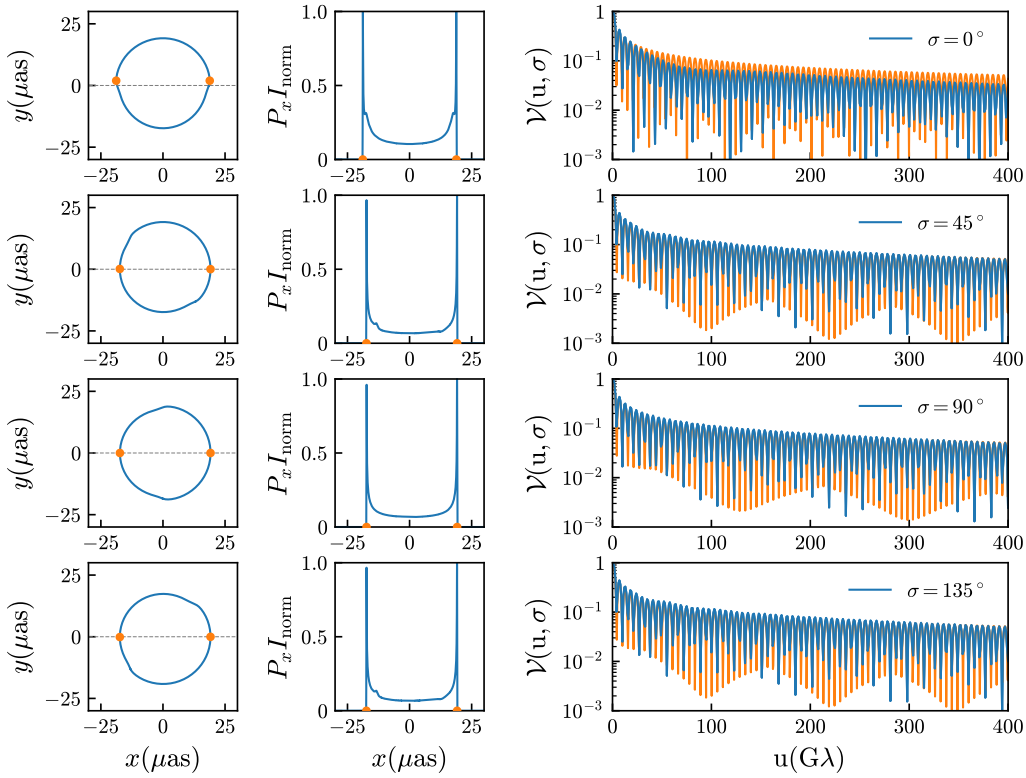

Fig. A1. Shape curve, normalized projected intensity $P_x I_{\rm norm}$, and (normalized) visibility $\mathcal{V}(u,\sigma)$ of the $n=3$ inner photon ring. The physical setup and color representation are the same as in Fig. 5.

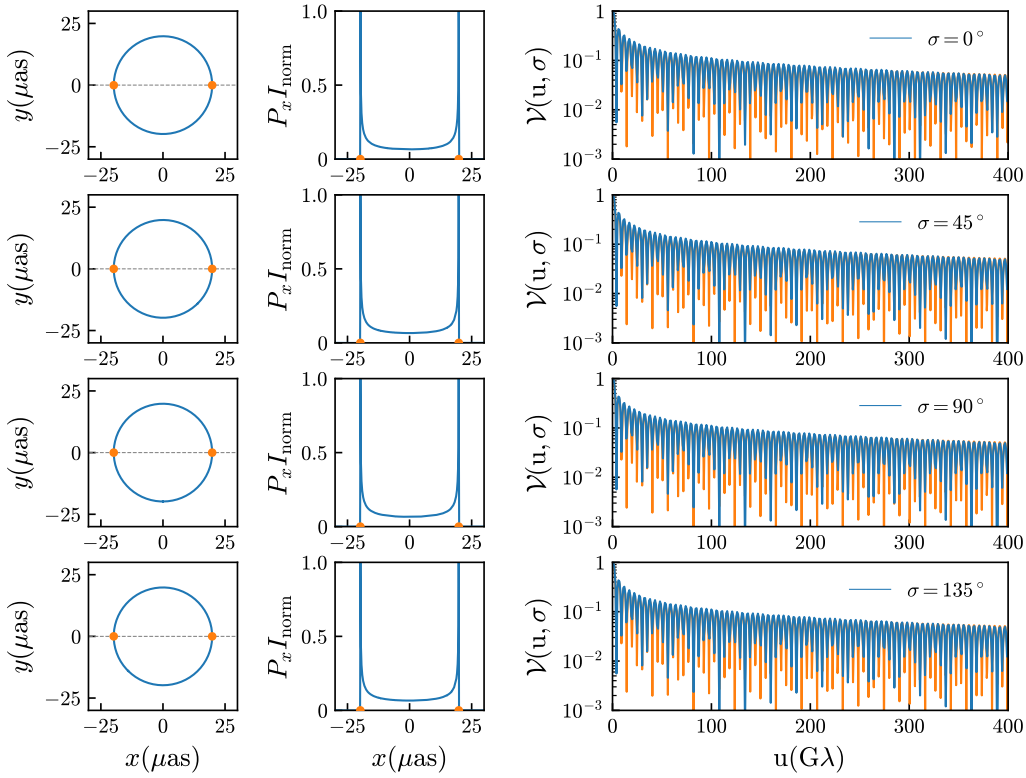

Fig. A2. Shape curve, normalized projected intensity $P_x I_{\rm norm}$, and (normalized) visibility $\mathcal{V}(u,\sigma)$ of the $n=3$ outer photon ring. The physical setup and color representation are the same as in Fig. 5.

References

[1] B. P. Abbott *et al.* (LIGO Scientific and Virgo Collaborations), Phys. Rev. Lett. **116**, 061102 (2016a)
[2] B. P. Abbott *et al.* (LIGO Scientific and Virgo Collaborations), Phys. Rev. X **6**, 041015 (2016b)
[3] B. P. Abbott *et al.* (LIGO Scientific and Virgo Collaborations), Phys. Rev. Lett. **116**, 241103 (2016c)
[4] B. P. Abbott *et al.* (LIGO Scientific and Virgo Collaborations), Phys. Rev. Lett. **118**, 221101 (2017a)
[5] B. P. Abbott *et al.* (LIGO Scientific and Virgo Collaborations), Astrophys. J. Lett. **851**, L35 (2017b)
[6] B. P. Abbott *et al.* (LIGO Scientific and Virgo Collaborations), Phys. Rev. Lett. **119**, 141101 (2017c)
[7] K. Akiyama *et al.* (LIGO Scientific and Virgo Collaborations), Astrophys. J. Lett. **875**, L1 (2019a)
[8] K. Akiyama *et al.* (LIGO Scientific and Virgo Collaborations), Astrophys. J. Lett. **875**, L2 (2019b)
[9] K. Akiyama *et al.* (LIGO Scientific and Virgo Collaborations), Astrophys. J. Lett. **875**, L3 (2019c)
[10] K. Akiyama *et al.* (LIGO Scientific and Virgo Collaborations), Astrophys. J. Lett. **875**, L4 (2019d)
[11] K. Akiyama *et al.* (LIGO Scientific and Virgo Collaborations), Astrophys. J. Lett. **875**, L5 (2019e)
[12] K. Akiyama *et al.* (LIGO Scientific and Virgo Collaborations), Astrophys. J. Lett. **875**, L6 (2019f)
[13] K. Akiyama *et al.* (LIGO Scientific and Virgo Collaborations), Astrophys. J. Lett. **930**, L12 (2022a)
[14] K. Akiyama *et al.* (LIGO Scientific and Virgo Collaborations), Astrophys. J. Lett. **930**, L13 (2022b)
[15] K. Akiyama *et al.* (LIGO Scientific and Virgo Collaborations), Astrophys. J. Lett. **930**, L14 (2022c)
[16] K. Akiyama *et al.* (LIGO Scientific and Virgo Collaborations), Astrophys. J. Lett. **930**, L15 (2022d)
[17] K. Akiyama *et al.* (LIGO Scientific and Virgo Collaborations), Astrophys. J. Lett. **930**, L16 (2022e)
[18] K. Akiyama *et al.* (LIGO Scientific and Virgo Collaborations), Astrophys. J. Lett. **930**, L17 (2022f)
[19] S. W. Hawking, Commun. Math. Phys. **43**, 199 (1975)
[20] S. D. Mathur, Class. Quant. Grav. **26**, 224001 (2009)
[21] V. Cardoso and P. Pani, Living Rev. Relativ. **22**, 4 (2019)
[22] K. Schwarzschild, Sitzungsber. Preuss. Akad. Wiss. Berlin (Math. Phys.) **1916**, 424 (1916)
[23] R. M. Wald, *General Relativity,* (University of Chicago Press, Chicago, 1984).
[24] V. Cardoso and P. Pani, Nat. Astron. **1**, 586 (2017)
[25] E. Berti, A. Sesana, E. Barausse *et al.*, Phys. Rev. Lett. **117**, 101102 (2016)
[26] S. E. Gralla, D. E. Holz, and R. M. Wald, Phys. Rev. D **100**, 024018 (2019)
[27] M. D. Johnson, A. Lupsasca, A. Strominger *et al.*, Sci. Adv. **6**, eaaz1310 (2020)
[28] F. H. Vincent, S. E. Gralla, A. Lupsasca *et al.*, Astron. Astrophys. **667**, A170 (2022)
[29] H. Paugnat, A. Lupsasca, F. H. Vincent *et al.*, Astron. Astrophys. **668**, A11 (2022)
[30] K. S. Virbhadra and G. F. R. Ellis, Phys. Rev. D **62**, 084003 (2000)
[31] V. Bozza, S. Capozziello, G. Iovane *et al.*, Gen. Relativ. Gravit. **33**, 1535 (2001)
[32] V. Bozza and G. Scarpetta, Phys. Rev. D **76**, 083008 (2007)
[33] R. Shaikh, P. Banerjee, S. Paul *et al.*, Phys. Rev. D **99**, 104040 (2019)
[34] A. O. Petters, Mon. Not. R. Astron. Soc. **338**, 457 (2003)
[35] F. Aratore and V. Bozza, J. Cosmol. Astropart. Phys. **10**, 054 (2021)
[36] Y.-X. Gao and Y. Xie, Eur. Phys. J. C **82**, 162 (2022)
[37] Y. X. Gao and Y. Xie, Phys. Rev. D **109**, 063030 (2024)
[38] Y. Chen, P. Wang, H. Wu *et al.*, J. Cosmol. Astropart. Phys. **2024**, 032 (2024)
[39] O. Y. Tsupko, Phys. Rev. D **106**, 064033 (2022)
[40] A. Cárdenas-Avendaño and A. Lupsasca, Phys. Rev. D **108**, 064043 (2023)
[41] F. Aratore, O. Y. Tsupko, and V. Perlick, Phys. Rev. D **109**, 124057 (2024)
[42] H. Jia, E. Quataert, A. Lupsasca *et al.*, Phys. Rev. D **110**, 083044 (2024)
[43] H. Falcke, F. Melia, and E. Agol, Astrophys. J. Lett. **528**, L13 (2000)
[44] P. V. P. Cunha and C. A. R. Herdeiro, Gen. Relativ. Gravit. **50**, 42 (2018)
[45] V. Perlick and O. Y. Tsupko, Phys. Rep. **947**, 1 (2022)
[46] V. Bozza, Phys. Rev. D **66**, 103001 (2002)
[47] M. Patil, P. Mishra, and D. Narasimha, Phys. Rev. D **95**, 024026 (2017)
[48] G. Gyulchev, P. Nedkova, T. Vetsov *et al.*, Eur. Phys. J. C **81**, 885 (2021)
[49] X. Y. Zhu and Y. Xie, Eur. Phys. J. C **80**, 444 (2020)
[50] T. Igata, M. Omamiuda, and Y. Takamori, Phys. Rev. D **111**, 084062 (2025)
[51] H. L. Tamm and J. a. L. Rosa, Phys. Rev. D **109**, 044062 (2024)
[52] G. J. Olmo, D. Rubiera-Garcia, and D. S.-C. Gómez, Phys. Lett. B **829**, 137045 (2022)
[53] J. L. Rosa, Phys. Rev. D **107**, 084048 (2023)
[54] S. Weinberg, *Gravitation and Cosmology: Principles and Applications of the General Theory of Relativity,* (Wiley, New York, 1972).
[55] K. S. Virbhadra, D. Narasimha, and S. M. Chitre, Astron. Astrophys. **337**, 1 (1998)
[56] P. V. P. Cunha, E. Berti, and C. A. R. Herdeiro, Phys. Rev. Lett. **119**, 251102 (2017)
[57] M. Guo and S. Gao, Phys. Rev. D **103**, 104031 (2021)
[58] P. V. P. Cunha, J. Grover, C. Herdeiro *et al.*, Phys. Rev. D **94**, 104023 (2016)
[59] J.-P. Luminet, Astron. Astrophys. **75**, 228 (1979)
[60] A. R. Thompson, J. M. Moran, and G. W. Swenson, *Interferometry and Synthesis in Radio Astronomy,* (Springer, Cham, 2017).
[61] S. E. Gralla, Phys. Rev. D **102**, 044017 (2020)
[62] S. E. Gralla and A. Lupsasca, Phys. Rev. D **102**, 124003 (2020a)
[63] H. Stephani, D. Kramer, M. MacCallum *et al., Exact Solutions of Einstein's Field Equations,* (Cambridge University Press, 2009).
[64] H. A. Buchdahl, Phys. Rev. **116**, 1027 (1959)
[65] L. Gabbanelli, J. Ovalle, A. Sotomayor *et al.*, Eur. Phys. J. C **79**, 486 (2019)
[66] J. Ovalle, C. Posada, and Z. Stuchlík, Class. Quant. Grav. **36**, 205010 (2019)
[67] P. Beltracchi and P. Gondolo, Phys. Rev. D **99**, 084021 (2019)
[68] P. O. Mazur and E. Mottola, Universe **9**, 88 (2023)
[69] P. O. Mazur and E. Mottola, Proc. Natl. Acad. Sci. **101**, 9545 (2004)
[70] C. Chirenti, C. Posada, and V. Guedes, Class. Quant. Grav.

37, 195017 (2020)
[71] R. A. Konoplya, C. Posada, Z. Stuchlík *et al*., Phys. Rev. D **100**, 044027 (2019)
[72] N. Sakai, H. Saida, and T. Tamaki, Phys. Rev. D **90**, 104013 (2014)
[73] F. Roelofs *et al*, Galaxies **11**, 12 (2023)
[74] D. Psaltis *et al*, Phys. Rev. Lett. **125**, 141104 (2020)
[75] Z. Zhang, Y. Hou, M. Guo *et al*., arXiv: 2503.17200[astro-ph.HE]
[76] Q. H. Zhu, arXiv: 2503.22343[astro-ph.HE]
[77] C. Posada, Mon. Not. R. Astron. Soc. **468**, 2128 (2017)
[78] J. L. Hernandez-Pastora and L. Herrera, Phys. Rev. D **95**, 024003 (2017)
[79] A. P. Ravi and N. Banerjee, New Astron. **64**, 31 (2018)
[80] H. Kim, B. Lee, W. Lee *et al*., Phys. Rev. D **101**, 064067 (2020)
[81] S. Viaggiu, Int. J. Mod. Phys. D **32**, 2350008 (2023)
[82] S. E. Gralla and A. Lupsasca, Phys. Rev. D **101**, 044031 (2020b)
[83] L. Zhou, Z. Zhong, Y. Chen *et al*., Phys. Rev. D **111**, 064075 (2025)